

LICHUN ZHAO¹, ZHIGUO LI², YONGJIE LIU³, YONGCHAO XU⁴,
P.L.P. WASANTHA⁵, XIAOBIN ZHENG², TAO XU^{2*}

STABILITY ANALYSIS OF OPEN-PIT BENCH SLOPE UNDER REPEATED HEAVY VEHICLE LOADING BASED ON STRESS-CORROSION MODEL

In the present study, we address an important and increasingly relevant topic in mining safety and efficiency, namely the stability of open-pit bench slopes subjected to daily heavy truck cyclic loading. Specifically, we focus on the stability of Zhahanur open-pit slope (Inner Mongolia region, China) and investigate the potential role of daily heavy truck cyclic loading in bench slope instability. To this end, we incorporate a stress corrosion model into the particle flow code to develop a time-dependent deformation model of the rock. With the established model, we quantitatively analyse the effect of heavy truck cyclic loading on the bench slope stability. Our results support the hypothesis that daily heavy truck loading can cause gradual downward deformation of a rock mass, leading to slope instability. To validate our numerical modelling results, we compare and analyse them with in situ monitoring data. Our study demonstrates the significant impact of daily heavy vehicles on bench slope stability in open-pit mines and provides a practical tool for assessing the long-term stability of open-pit bench slopes and optimising mining operations.

Keywords: open-pit slope; stress-corrosion model; cyclic loading; particle flow code; bench slope stability

1. Introduction

The working benches in open-pit mines are crucial for continued operation and efficient ore production. Typically, heavy trucks operating on working benches are generally used for loading and hauling in open-pit mines such as the Zhahanur open-pit coal mine, in Jarud Banner, eastern

¹ FACULTY OF ENGINEERING, CHINA UNIVERSITY OF GEOSCIENCES, WUHAN, HUBEI 430074, CHINA & JARUD BANNER ZHAHANUR COAL INDUSTRY CO. LTD, JARUD BANNER 029100, CHINA

² SCHOOL OF RESOURCES AND CIVIL ENGINEERING, NORTHEASTERN UNIVERSITY, SHENYANG 110819, CHINA

³ COAL MINE CENTER, SPIC INNER MONGOLIA ENERGY CO. LTD., INNER MONGOLIA, CHINA

⁴ JARUD BANNER ZHAHANUR COAL INDUSTRY CO. LTD, JARUD BANNER 029100, CHINA

⁵ COLLEGE OF SPORT, HEALTH AND ENGINEERING, VICTORIA UNIVERSITY MELBOURNE, VIC 3011, AUSTRALIA

* Corresponding author: xutao@mail.neu.edu.cn



© 2024. The Author(s). This is an open-access article distributed under the terms of the Creative Commons Attribution-NonCommercial License (CC BY-NC 4.0, <https://creativecommons.org/licenses/by-nc/4.0/deed.en>) which permits the use, redistribution of the material in any medium or format, transforming and building upon the material, provided that the article is properly cited, the use is noncommercial, and no modifications or adaptations are made.

Inner Mongolia, China, which serves as the case study mine site of the present study. Repeated travelling of heavy trucks can be detrimental to the integrity of working benches, resulting in slope failures. Notably, fractures were observed on the working bench slope at 920 m and 944 m above sea level in the Zhahanur open-pit coal mine. These fractured benches are the primary working benches of the mine, and numerous heavy trucks transport on the benches every day.

The influence of the vehicle load on the damage to the road surface or pavement gradually accumulates with the repeated running time of the vehicle has been studied. Extensive data from various types of vehicles have been analysed to identify their load characteristics and influence on road surfaces and pavements. The American Association of Highway and Transportation Officials was one of the first organisations to investigate the effects of vehicle loads on pavement damage and proposed the well-known fourth power law based on a series of road tests under different vehicle loadings. The relationship between the tyre model and the road surface is usually assumed as the point contact in the theoretical study of vehicle dynamics [1]. To match the actual vehicle-road interaction, the point contact model has been developed into the line contact model and surface contact model. Various researchers have proposed and studied different models for the vehicle-road interaction, including a flexible roller contact tyre model [2] simplified vehicle loads as an equivalent static concentrated load [3], and the influence of different vehicle speeds on the dynamic response of road surfaces. [4] studied the influence of different vehicle speeds on the dynamic response of a road surface and reported that the dynamic load of vehicles on the road surface increases with an increase in speed. Under the same conditions, the dynamic load of heavy vehicles on the road surface is significantly larger than that of light vehicles, and the potential damage caused by heavy vehicles on the road surface can be severe. All of these studies confirm that vehicle loads have a significant effect on dynamic response, and heavy vehicles can cause severe potential damage to road surfaces. Moreover, the stability safety factor of underground structures increases relatively after considering dynamic loading. Therefore, the effect of cyclic dynamic vehicle loading on the stability of excavation or rock slopes cannot be ignored.

Laboratory testing is an effective approach to analysing failure behaviour and the mechanism of slopes under cyclic dynamic loading conditions. A range of shaking table tests was conducted to investigate the mechanisms of cyclic dynamic-induced permanent deformation and failure behaviour in slopes [5,6]. However, the scale of laboratory tests on a shaking table is limited to the size of the table, which can restrict the size of structures that can be tested, and laboratory tests using a shaking table can be expensive since specialised equipment and trained personnel are needed to operate these devices. Moreover, it can be challenging to control the intensity of the shaking table, which may limit the accuracy of the results obtained.

With the development of computers, numerical techniques have also become more accurate and reliable. This reliability has enabled numerical simulations to be used in many practical applications. It has also become essential for evaluating the behaviour of rock mass and rock structures under complex loading conditions. The finite element method (FEM) is a powerful computational tool that provides a flexible, accurate, cost-effective, and time-efficient means of solving complex problems in engineering and physics. Its versatility and effectiveness make it a widely used tool in many fields of study. FEM with limit analysis was applied in the analysis of slope stability to provide rigorous lower and upper bounds to the exact critical load [7], and the finite-element limit analysis method was used in the evaluation of the aseismic stability of slopes [8]. [9] used the virtual proving ground approach for obtaining the dynamic stress or strain history and distribution and performed dynamic stress analysis of the vehicle frame using a non-

linear finite element method. [10] implemented nonlinear shear strength criteria of power-law type in a finite element model and performed FEM analysis of slope stability using limit analysis and limit equilibrium approach. [11] presented a numerical limit analysis on the slope stability using the rigid finite element method with the consideration of the rotational component of the centroid velocity for each element, as well as a generalised overturning failure criterion governing the element rotation. [12] used a finite element method to discuss the dynamic response of compacted loess subgrade under dynamic load, established a numerical calculation model, and deduced a deformation law of loess subgrade with different compaction degrees. [13] developed a finite element limit analysis method with a pseudo-static approach to assess the seismic stability of earth-rock dams and determined the lower and upper bounds on the critical seismic coefficients of dams. [14] carried out finite element analysis by utilising a multibody systems approach to vehicle dynamics. [15] studied the slope stability under the combined action of rainfall and vehicle based on the limit equilibrium method.

Although FEM has been widely used in rock mechanics and engineering studies, it still has some limitations when applied to the analysis of highly heterogeneous and discontinuous rock mass. In contrast, the Discrete Element Method (DEM) has been proven to be a suitable tool for studying rock mechanics under highly heterogeneous conditions due to its capability of explicitly considering the local interactions between individual elements of the materials. DEM has been successfully applied in dealing with highly discontinuous rock mass behaviour, such as crack propagation and coalescence in the step-path failure mechanism of rock [16]. The landslide evolution process of the open-pit mine and the unloading scheme of the mine slope were also investigated using DEM [17,18]. [19] studied the vehicle-asphalt pavement interaction and micro-structure by discrete element method, and [20] performed discrete element modelling of the meso-mechanical response of asphalt pavement under vehicle load. Existing studies have shown that vehicles have a great influence on slope stability, and that vehicle loading on the slope is mainly set as static or dynamic loading. However, in reality, the loading of vehicles on the slope is cyclic, as the vehicle repeatedly operates on bench roads. The deformation of a rock mass subjected to cyclic repeated loading differs from that under static loading conditions [21-25]. Therefore, it is of great significance to gain insight into the mechanism of bench slope stability under repeated heavy vehicle loading. In the present manuscript, we first described a model to couple the stress corrosion theory with a discrete element method, Particle Flow Code, accounting for the influence of stress corrosion. Then a set of laboratory experiments were conducted, and the simulation results were compared with the experimental data to validate and calibrate the model. Furthermore, we evaluated the safety and durability of the slope under the influence of stress corrosion by applying the calibrated model to the slope stability analysis under repeated heavy vehicle loading and gained a comprehensive understanding of the deformation behaviour of the slope under repeated heavy vehicle loading.

2. Stress-corrosion incorporated particle flow model

Stress corrosion, also known as stress corrosion cracking, is a type of corrosion that occurs owing to the simultaneous action of a corrodent and sustained tensile stress. It's a phenomenon that when the load on the rock is between the peak compressive strength and the stress corrosion threshold, the mechanical properties of the rock continue to weaken over time and, finally,

instability failure occurs. It has been recognised that stress corrosion is likely the main mechanism of subcritical crack growth under shallow crustal conditions [26]. Stress corrosion causes damage accumulation in rocks, leading to time-dependent deformation [26,27]. Based on the time-dependent deformation induced by stress corrosion, a numerical model of time-dependent deformation and damage of rock was established in this study by incorporating the parallel-bonded stress corrosion model into the particle flow code (PFC) to investigate the deformation behaviours of the northern slope of the Zhahanur open-pit coal mine under daily heavy truck loading. The simulation results were compared with the on-site monitoring data. Overall, the results of this study provide some theoretical guidance for bench slope management in surface mining, such as the northern slope of Zhahanur open-pit coal mine.

2.1. Parallel bond model

Particle Flow Code (PFC) is a distinct-element modelling (DEM) framework proposed by Cundall and Strack [28]. PFC models synthetic materials composed of an assembly of variably-sized rigid particles that interact at the contacts to represent both granular and solid materials. Each particle in the PFC model is denoted as a body and not a point mass. A general particle-flow model simulates the mechanical behaviour of a system consisting of a collection of arbitrarily shaped particles. PFC models simulate the independent movement (translation and rotation) and interaction of many rigid particles that may interact at contacts based on an internal force and moment. Contact mechanics obey particle-interaction laws that update the internal forces and moments. Force transfer satisfies Newton's law, and it is convenient to deal with the mechanical problems of discontinuous media.

The parallel bond model provides two types of contact interfaces. The first contact interface is equivalent to the linear model and regulates slip by applying a Coulomb limit to the shear force and is capable of transmitting both force and friction between particles. The second contact interface is resistant to relative rotation, and its behaviour is linearly elastic. When the contact force exceeds the strength limit, the bond breaks and degenerates into a linear model, meanwhile, it can transmit both force and moment between the particles. A schematic of the parallel bond model is represented in Fig. 1. Owing to the relative motion among particles, the bond is affected by the force and moment. The parallel bond model requires setting the normal and tangential bond strengths. When the normal stress at the contact is greater than the normal bond strength or the tangential stress is greater than the tangential bond strength, the bond will break, and the mechanical parameters such as force and stiffness at the bonding point will be reduced to zero. The normal and tangential stresses can be calculated using equations (1) and (2).

$$\bar{\sigma} = \frac{-\bar{F}_i^n}{\bar{A}} + \frac{|\bar{M}_i^s|}{\bar{I}} \bar{R} \quad (1)$$

$$\bar{\tau} = \frac{|\bar{F}_i^s|}{\bar{A}} + \frac{|\bar{M}_i^n|}{\bar{J}} \bar{R} \quad (2)$$

where, $\bar{\sigma}$, $\bar{\tau}$ are the normal stress and tangential stress at the contact; \bar{R} is the radius of bond, \bar{A} , \bar{I} , \bar{J} are respectively the parallel bond area, and the parallel bond rotational inertia, the parallel bond polar inertia.

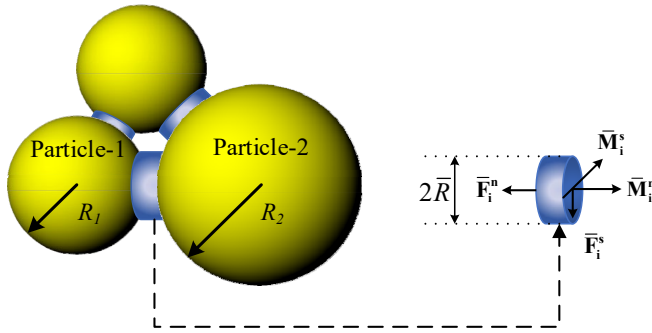


Fig. 1. Schematic representation of the parallel bond contact model (\bar{F}_i^n and \bar{F}_i^s are normal contact forces and tangential contact force, respectively; \bar{M}_i^n and \bar{M}_i^s are normal and tangential contact moments, respectively; \bar{R} is the radius of the bond)

$$\begin{aligned}
 \bar{R} &= \begin{cases} \min(R_1, R_2), & \text{ball-ball} \\ R_1, & \text{ball-wall} \end{cases} & \bar{A} &= \begin{cases} 2\bar{R}t, & 2D \quad (t=1) \\ \pi\bar{R}^2, & 3D \end{cases} \\
 \bar{I} &= \begin{cases} \frac{2}{3}t\bar{R}^3, & 2D \quad (t=1) \\ \frac{1}{4}\pi\bar{R}^4, & 3D \end{cases} & \bar{J} &= \begin{cases} 0, & 2D \\ \frac{1}{2}\pi\bar{R}^4, & 3D \end{cases}
 \end{aligned} \tag{3}$$

The Mohr-Coulomb criterion is used to determine the failure behaviour in the parallel bond model, and some macro-mechanical parameters, such as tensile strength, cohesion, and the angle of internal friction, need to be set at the contacts. The envelope of the parallel bond strength in terms of the Mohr-Coulomb criterion is represented in Fig. 2.

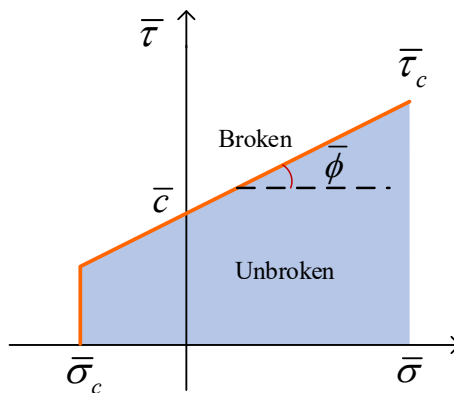


Fig. 2. Envelope of parallel bond strength (In the parallel bond model, when the stress at the contact exceeds the threshold, the bond breaks, and the program automatically sets the values of mechanical parameters such as force, moment and stiffness at the contact to zero), $\bar{\phi}$ is the angle of internal friction, \bar{c} is the cohesion, $\bar{\sigma}_c$, and $\bar{\tau}_c$ are the normal strength and tangential strength at the contact, respectively

2.2. Stress-corrosion model

Stress corrosion, a weakening reaction of a bond in rock materials by a chemical reaction, is considered one of the key factors driving the time-dependent behaviour of rocks in the upper crust. This complex behaviour of rock materials can be revealed by incorporating the microstructure into a rock model. For example, different microscopic characteristics are assigned to the bonding interface between the particles in the PFC, and the effect of stress corrosion is reflected by changing the physical parameters of the bonds. Previous studies, for instance, [29-31], introduced stress corrosion theory into the particle flow code (PFC) and shortened the contact length between different particles in the model to mimic time-dependent weakening processes in rock at the microscale. The contact diameter, D , between particles is reduced to weaken the contact strength between the particles. When the stress between the particles is between the stress corrosion threshold and the tensile strength of the bond, the contact diameter between particles continues to decrease with time. During the entire servo process, the contact force between the particles is constantly updated. The stress corrosion model and the corrosion rate curves are shown in Fig. 3.

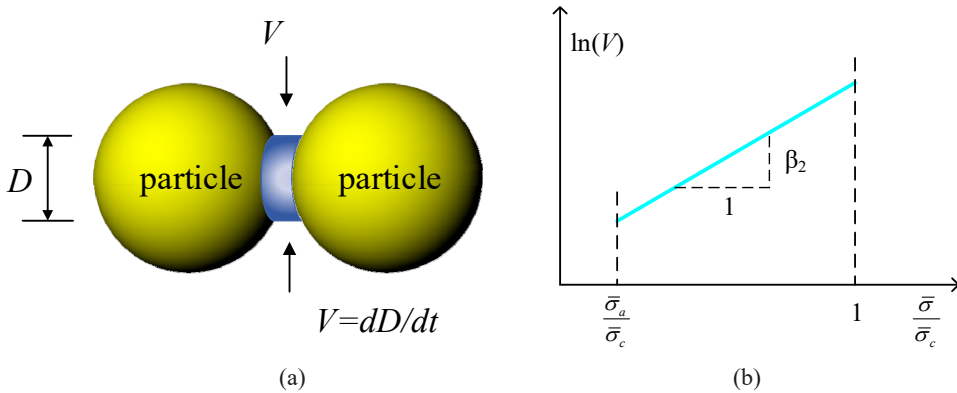


Fig. 3. Stress corrosion model. (a) Schematic of stress corrosion model, (b) Corrosion rate curve

In the stress corrosion model, the stress corrosion rate is expressed by Equation 4.

$$\frac{d\bar{D}}{dt} = \begin{cases} 0 & \bar{\sigma} \leq \bar{\sigma}_a \\ -\beta_1 e^{\beta_2 \left(\frac{\bar{\sigma}}{\bar{\sigma}_c} \right)} & \bar{\sigma}_a \cdot \bar{\sigma} \cdot \bar{\sigma}_c \\ -\infty & \bar{\sigma} \geq \bar{\sigma}_c \end{cases} \quad (4)$$

where $\bar{\sigma}$ is the maximum tensile stress at the contact of parallel bonds between particles, $\bar{\sigma}_a$ is the stress threshold, $\bar{\sigma}_c$ is the tensile strength of parallel bonds between particles, \bar{D} is the diameter of parallel bonds, β_1 and β_2 are material constants.

3. Model parameter calibration

The particle flow code (PFC) is based on local contacts to reflect macro-mechanical properties. Only the geometric and mechanical parameters of the particles and contacts must be defined in the simulation [21]. However, there is no effective method to determine the relationship between macro-parameters and micro-parameters, and the micro-parameter assignment of the particle flow code can only be calibrated by trial and error method [32]. PFC reflects the macroscopic mechanical properties of the model from a microscopic perspective. Therefore, it is necessary to calibrate the parameters for different properties of the studied slope.

The northern slope of Zhahanur open pit coal mine is an anti-inclined layered rock slope with a designed overall slope angle of 22° . By analysing the distribution of different lithologies in the drilled borehole cores and combining with the results obtained in previous research, the strata of the open-pit coal mine can be mainly classified into six lithologies, namely waste dump, Quaternary strata, Tertiary strata, mudstone, coal seam, and sandstone. According to previous investigations, the mechanical parameters of Quaternary strata, Tertiary strata and mudstone on the northern slope of Zhahanur open-pit coal mine are listed in TABLE 1. A biaxial compression specimen model was established based on the particle size of the slope model. Numerical biaxial compression on the specimen, under different confining pressures, was performed to obtain the cohesion and internal friction angle of the model based on the macroscopic rock mass. The width of the specimen should exceed 40 times the average particle size to avoid size effect during the parameter calibration. The numerical biaxial compressive model is presented in Fig. 4.

TABLE 1

Mechanical parameters of Quaternary strata, Tertiary strata and mudstone
in the north slope of Zhahanur open-pit coal mine

Properties	Unit weight γ (kN/m ³)	Cohesion c (kPa)	Angle of internal friction ϕ (°)
Quaternary strata	17.7	30	5.7
Tertiary strata	17.7	32	6.5
Mudstone	20.2	33.7	15.4

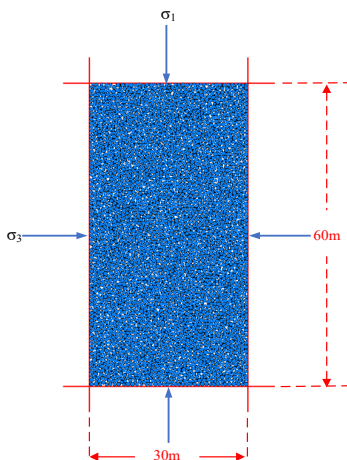


Fig. 4. Numerical biaxial compressive model. (The model is 60 m in height and 30 m in width, and confining pressure is applied to the left and right walls, while the upper and lower loading serves as axial servo-control. The walls enable applying velocity boundary conditions to assemblies of balls or clumps for compaction and confinement purposes in PFC)

The microscopic parameters of the model were calibrated using a trial-and-error method. Initially, biaxial compressions on the specimen under confining pressures of 0, 10, 20, and 30 kPa were conducted, to obtain the peak strength under different confining pressures. The Mohr circle and strength envelope were developed, until the cohesion and internal friction angle of the model were consistent with the macroscopic mechanical parameters of Quaternary strata, Tertiary strata, and mudstone, respectively. This allowed us to obtain the microscopic parameters of the corresponding rock. Furthermore, time-sensitive microscale parameters in the stress corrosion model were calibrated based on relevant rock mechanics experiments. For instance, taking Tertiary strata as an example, Figs. 5 and 6 depict the complete stress-strain curves and Mohr strength envelope of the Tertiary strata rock under different confining pressures.

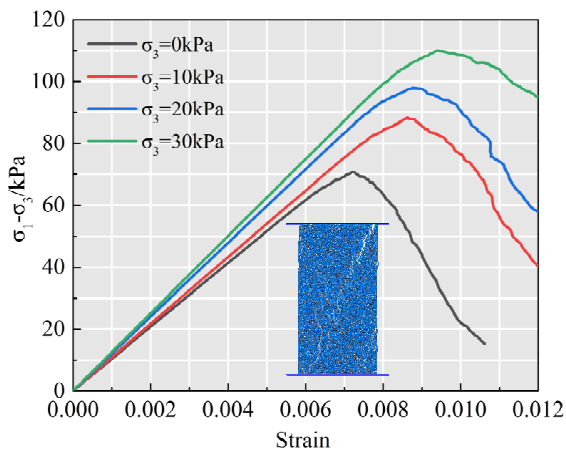


Fig. 5. Complete stress-strain curves of the Tertiary strata rock under different confining pressures

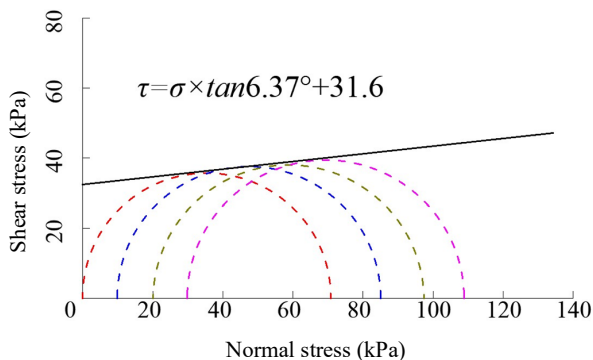


Fig. 6. Mohr circles and the Mohr strength envelope of the Tertiary strata rock under different confining pressures

Figs. 5 and 6 show that the elastic modulus and peak strength of the rock model both increased with an increase in confining pressure, and shear failure occurred in the specimen. It can

be seen from Fig. 6 that the cohesion of the rock model is 31.6 kPa, and the angle of internal friction is 6.37° , which is consistent with the macroscopic mechanical parameters of the Tertiary strata. Therefore, we conclude that the microscopic parameters meet the simulation requirements. Following the same procedure, we calibrated the microscopic parameters of Quaternary strata and mudstone, as presented in TABLE 2.

TABLE 2

Microscopic parameters of numerical model

Parameters	Friction coefficient	Contact modulus E^*/kPa	Stiffness ratio k^*	Parallel-bond tensile strength $\bar{\sigma}_c/\text{kPa}$	Parallel-bond cohesion \bar{c}/kPa	Parallel-bond internal friction angle $\bar{\phi}$	Material constant $\beta_1/10^{-12}$	Material constant $\beta_2/10^{-12}$
Quaternary	0.1	6	1	38	34	8	21.4	15.2
Tertiary	0.1	5	1	41	35	10	19.7	14.5
Mudstone	0.1	8	1	50	48	9.5	17	12.6

4. Case study

4.1. Site description

The Zhahanur open-pit coal mine is located in the northwest of Tongliao city, Inner Mongolia, China, covering an area of approximately 60 km in length (east-west) and 10 km in width (north-south). In 2020, the waste dump in the northern slope of the mining area suffered from a significant failure, which was triggered by the damage caused by the drainage holes at the 920 m and 944 m levels. Visible fractures can be seen at the slope, as illustrated in Fig. 7, which posed a significant risk to the production of the open-pit coal mine. According to on-site statistics, the bench width at the 920 m level is designed to be 30 m, and 55 100-ton trucks are transported daily. Conversely, the bench width at the 944 m level is designed to be 150 m, of which 30 m



Fig. 7. Fractures appeared on the surface of the transportation bench. (a) Induced fractures at the 920 m level. (b) induced fractures and slope deformation at the 944 m level

is for the road, and the remaining width serves as a safety distance, and 150 80-ton trucks daily transport alongside the bench. The recurring operation and transportation of heavy trucks generate cyclic loading, which induces potential damage and instability in the slope. Therefore, it is necessary to study the impact of daily heavy truck loading on the stability of the bench slope in the northern part of the open-pit coal mine.

4.2. Numerical model

A cyclic loading model of the northern slope of Zhahanur Open-pit mine was established using PFC to analyse the deformation behaviour of the bench slope under the cyclic loading of daily heavy trucks. Fig. 8 shows the spatial locations of 13 cross-sections across the northern slope of the mine. The radar monitoring data showed that the most significant deformation occurred near the slope of the NB-4 cross-section. Therefore, we selected the NB-4 cross-section slope as the primary object for analysis, and a cross-sectional view of the slope is shown in Fig. 9. The lithology involves a Quaternary stratum located at the 944 m level and a Tertiary stratum located at the 920 m level. The slope model was established based on the NB-4 cross-section, and the particles in the slope model were grouped according to different lithologies. The numerical slope model is shown in Fig. 10. Due to the large size of the slope and the limitation of computer power,

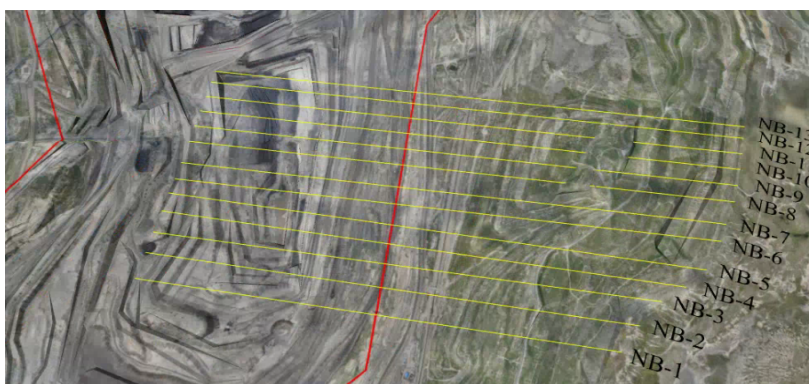


Fig. 8. Spatial location of 13 cross-sections cross the north slope of the mine (Thirteen cross-sections, NB-1 to NB-13, are arranged across the north slope)

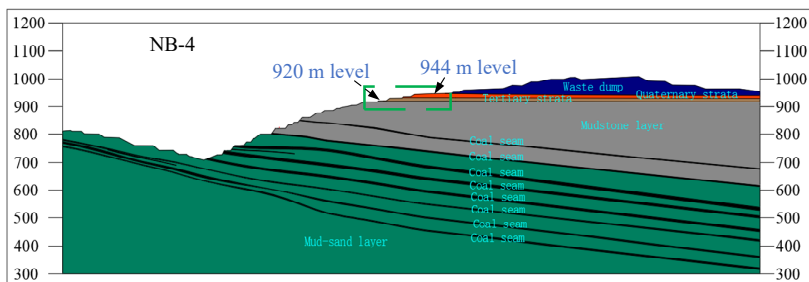


Fig. 9. The north slope of the NB-4 cross-section

it is necessary to significantly increase the radius of the particles in the slope model. However, it is challenging to maintain accuracy while increasing the particle radius. Therefore, we chose a subsection of the slope (red box in Fig. 10) to create the slope model for analysis. The distribution of lithology of the slope model for analysis is illustrated in Fig. 11; heavy trucks passed through the 920 m and 944 m levels, and the 913 m level, 928 m and 935 m levels did not pass through the heavy trucks.

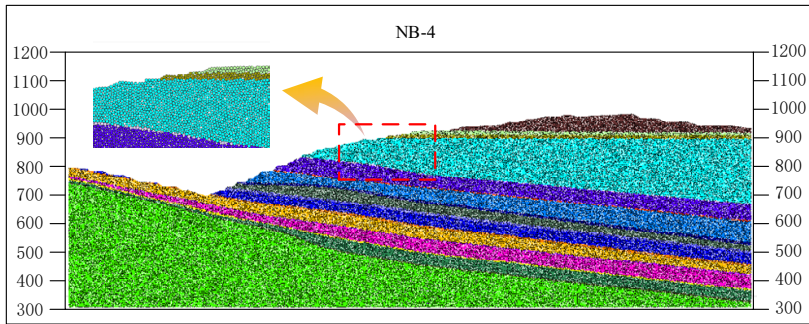


Fig. 10. The particle flow slope model of NB-4 cross-section, and subsection in the red box is selected for analysis

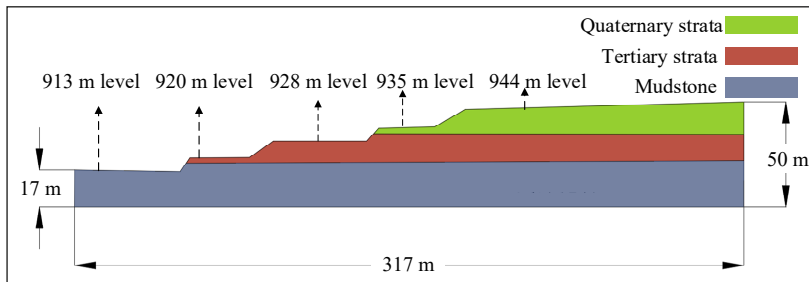


Fig. 11. The distribution of lithology of the slope model for analysis

We selected the radius distribution of particles using the trial-and-error method, and the chosen distribution range was between 0.3 and 0.45 m. Initially, we generated particles within the scope of the model, and then allowed them to settle under gravity until they reached mechanical equilibrium. The suspended particles in the model were subsequently deleted, and effective particles were allocated using a linear parallel bond model. To ensure even load distribution on the benches, we established loading walls at the 920 m and 944 m levels, and subsequently grouped the particles based on the distribution of lithologies, as illustrated in Fig. 12a. Altogether, the model is comprised of 21928 particles representing the three strata, namely Quaternary, Tertiary, and mudstone. We observed the force chain distribution of the model under gravity as shown in Fig. 12b. When at the same elevation, the thicker the overlying strata, the larger the contact force between the particles. Our model also features twelve monitoring points on different benches to monitor real-time displacement in the current state, and their positions are depicted in Fig. 12c.

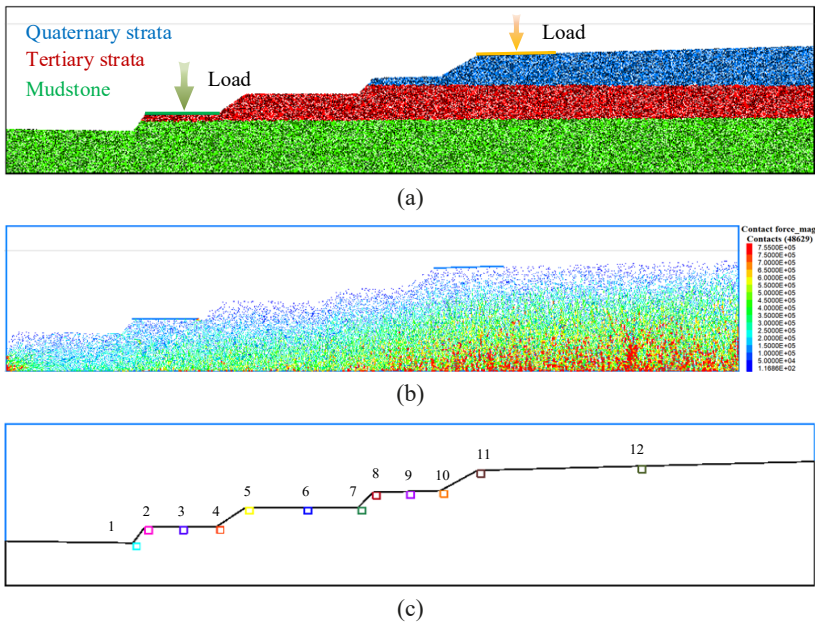


Fig. 12. Local slope model of particle flow code (a) Slope model and particle grouping, (b) Distribution of contact force chains under gravity, and (c) Position of twelve monitoring points along the benches

4.3. Numerical simulations

Due to limitations in numerical calculations, we transformed the loading of heavy trucks into a load on the loading walls of the model in this study. Consequently, we considered only the cyclic loading of heavy trucks, with the path of cyclic loading on the bench slope depicted in Fig. 13.

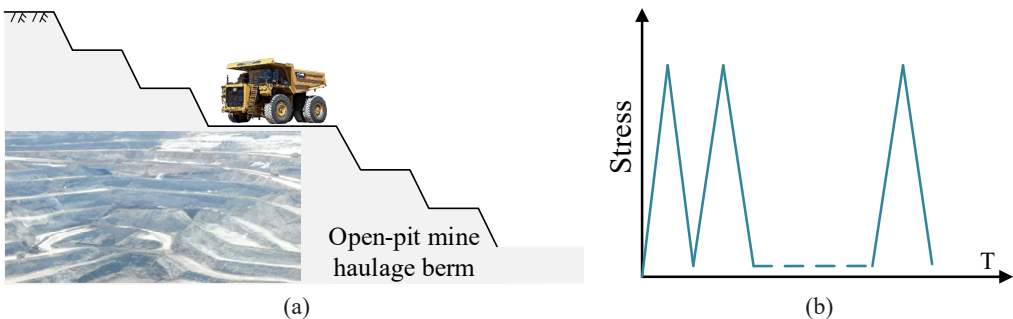


Fig. 13. (a) Schematic of the bench slope with heavy truck loading, and (b) the path of cyclic loading on the bench slope used in the modelling

The benches are subjected to dynamic load when heavy trucks drive through them. The ratio of the dynamic load to the static load is referred to as the dynamic load coefficient. In open-pit

mining, pavements are classified into four grades, namely A, B, C, and D. The dynamic load coefficients of the A-, B-, C-, and D-grade pavements are 1.12-1.19, 1.23-1.38, 1.48-1.76, and 2.00-2.52, respectively. We used a dynamic load coefficient of 1.15 for the pavements at the 920 m and 944 m levels of the Zhahanur open-pit mine due to their relatively flat nature. Based on the weight and number of heavy trucks passing through the benches, we designated a defined loading scheme. The servo stress at the 920 m level was loaded 55 times with a value of 230 kPa, while the servo stress at the 944 m level was loaded 150 times with a value of 184 kPa.

Slope stability is assessed based on the following three aspects: 1) if the model calculation does not converge, the slope is deemed unstable, 2) the formation of macroscopic cracks in the model indicates an unstable state of the slope, and 3) when the slope displacement exceeds 1 m, it is considered unstable. We recorded the maximum displacement curves of twelve monitoring points in the current state, as depicted in Fig. 14.

Fig. 14 illustrates that the largest displacement of 0.13 m occurred at monitoring point 11 on the 944 m level while monitoring points 2 and 3 on the 920 m level recorded the maximum displacement of 0.04 m. The displacement of the benches that were not haulage berms from the other monitoring points was 0.02 m, indicating that the slope is generally stable. The large deformations observed on the slope at the 920 m and 944 m levels aligned well with the numerical simulation results. Furthermore, the radar monitoring data, represented in Fig. 15, show that the single-day displacement at the 913 m level is approximately 20 mm, which closely corresponds with the deformation estimated from the numerical model.

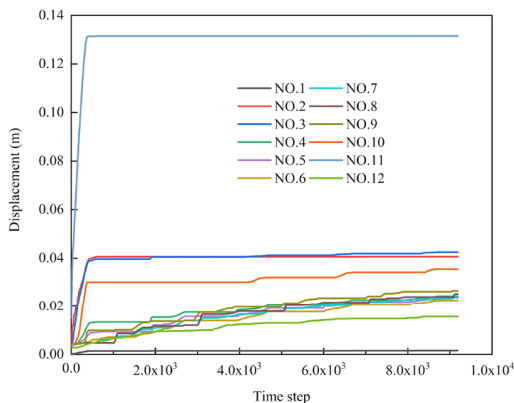


Fig. 14. Maximum displacement of twelve monitoring points along the slope under cyclic loading

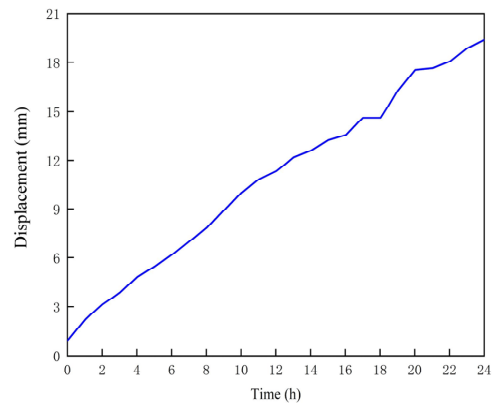


Fig. 15. Single-day radar monitoring displacement at the 913 m level

4.4. Time-dependent deformation and stability

The simulation results indicate a significant local displacement at the 920 m and 944 m levels caused by self-weight and cyclic loading, yet the slope as a whole remains stable. The magnitude of the material constant (i.e. β_1 , β_2) in the parallel-bonded stress corrosion (PSC) model directly determines the weakening rate of the rock mass strength. To further examine the potential sliding mass under cyclic loading, we adjusted the material constants (β_1 , β_2) in the PSC model to accelerate the weakening of rock mass strength of the slope. The displacement and

deformation at each monitoring point on the slope were recorded until the instability criterion for the slope was met. The simulations for different material constants are shown in Fig. 16. It can be observed that the displacement of each monitoring point increases continually with an increase in the material constant. When the magnification of material constant (β_1, β_2) is less than 1.15, the local position of the slope exhibits significant deformation. However, with the mutual dislocation of the internal particles and the redistribution of the contact force, the maximum displacement of each monitoring point eventually stabilises, indicating that the slope as a whole is stable. When the magnification of material constant (β_1, β_2) is 1.15, the displacement of monitoring point 11 does not converge. Continuous cyclic loading results in the maximum displacement at the shoulder at the 944 m level reaching 1 m, causing the calculation to terminate. Additionally, the deformation at the 920 m level is noticeable. As the magnification continues to increase, when it reaches 1.2, the displacement at the 920 m level changes abruptly, except for the 944 m level. At this point, both the 920 m and 944 m levels are damaged, resulting in the termination of calculations.

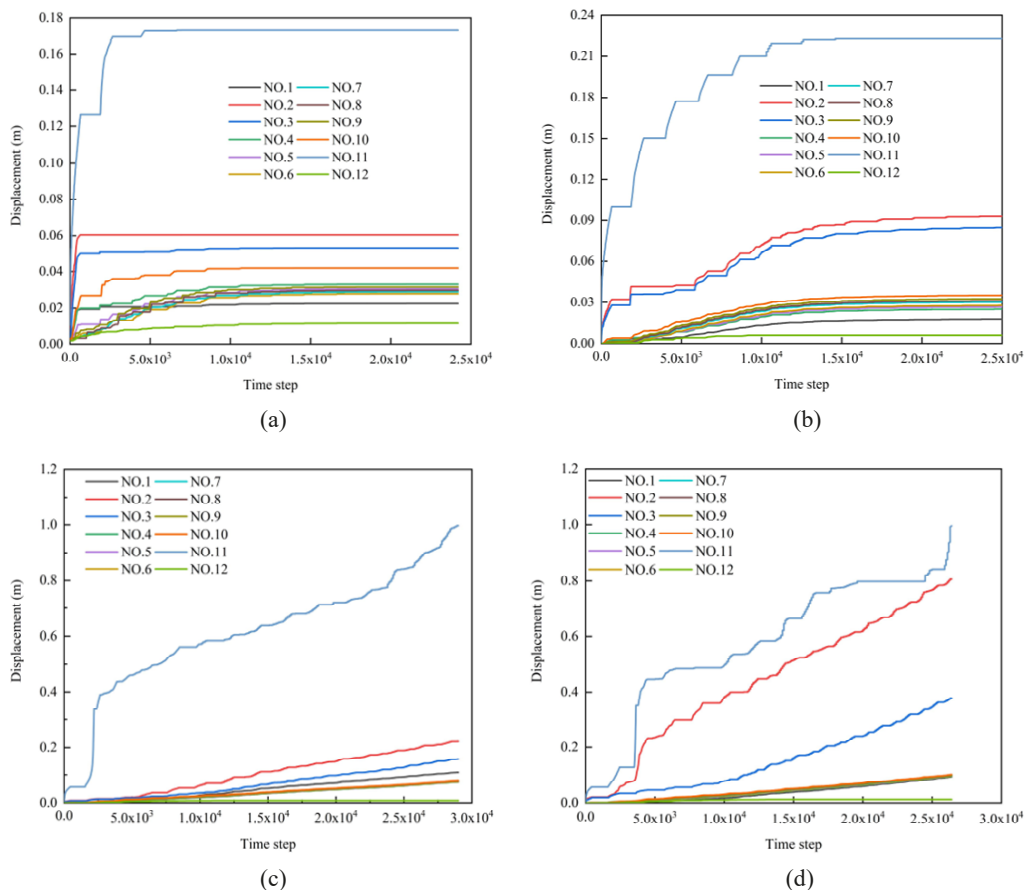


Fig. 16. Displacement curves when the magnification of material constant (β_1, β_2) is (a) 1.05, (b) 1.1, (c) 1.15, and (d) 1.2

Fig. 17 shows the slope displacement with the magnification of material constant (β_1, β_2) of 1.15. Under the influence of gravity and cyclic loading, noticeable deformation occurs at the shoulder of the 944 m level, and the coalescence of cracks forms a shallow sliding body. However, there is only some deformation near the slope at the 920 m level, with no sliding body formed. Figure 18 shows the displacement of the slope as a whole and in different directions with the magnification of material constant (β_1, β_2) of 1.2. Fig. 18 indicates that under the effect of gravity and cyclic loading, the slope at the 920 m level and the 944 m level exhibits significant deformation and forms sliding bodies, respectively. Deformations at the 944 m level still occur within the benches, with larger deformation values and ranges than those of the magnification

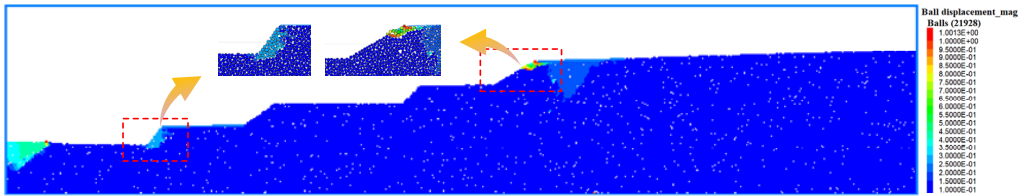
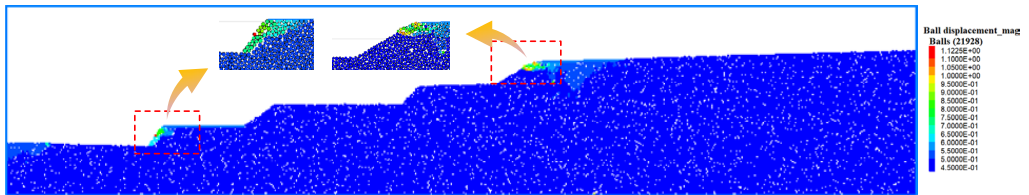
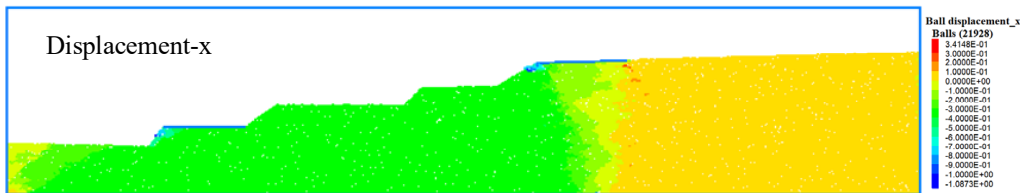


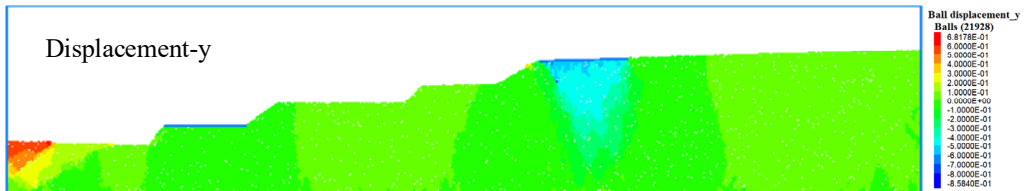
Fig. 17. The slope displacement when the magnification of material constant (β_1, β_2) is 1.15



(a)



(b)



(c)

Fig. 18. Displacement nephogram of the slope when the magnification of material constant (β_1, β_2) is 1.2.
 (a) The slope displacement, (b) The slope displacement in X direction,
 and (c) The slope displacement in Y direction

at 1.15. On the other hand, deformation at the 920 m level occurs on the bench surface. This is because the strata at the 944 m level are mostly Quaternary, generally softer, with a small bench angle, which results in the deformation mainly occurring within the bench and a complete landslide being difficult to form. Meanwhile, the lithology of the 920 m level is mainly composed of Tertiary and mudstone, with higher strength than that of the Quaternary. Additionally, the slope angle at the 920 m level is greater than that of the 944 m level. With the continuous weakening of the mechanical strength of slope rock mass, large-scale sliding will eventually occur. As the 944 m level strata are Quaternary, the daily heavy truck loading causes vertical deformation that is more pronounced than that of the 920 m level.

5. Discussion

Various factors, such as geotechnical properties, hydrogeology, geomorphological conditions, climate, weathering, vegetation, and human engineering activities, can impact slope stability [33–40]. The findings of our study reveal that the cyclic loading of heavy vehicles can cause noticeable deformation of the benches, leading to the production of cracks in the field. Accordingly, it is pertinent to investigate whether the cracks observed at the 944 m and 920 m levels of the Zhahanur open-pit mine were due to the action of heavy vehicle loading. Therefore, we conducted several surveys in the study area of the Zhahanur open-pit mine, with a portion of the benches on the north side depicted in Fig. 19. We established GNSS (Global Navigation Satellite System) monitoring point JCD01 at the 920 m level and monitoring point JCD02 at the 935 m level. We measured daily deformation at two monitoring sites from August 1, 2021, to August 30, 2021. The monitoring curves are shown in Fig. 20. All three monitoring sites exhibited deformation, with the deformation at the 920 m level significantly higher than that of the 935 m level. We infer that the deformation at the 935 m level, without vehicle passages, was solely generated under the influence of gravity, while the combined action of gravity and vehicle

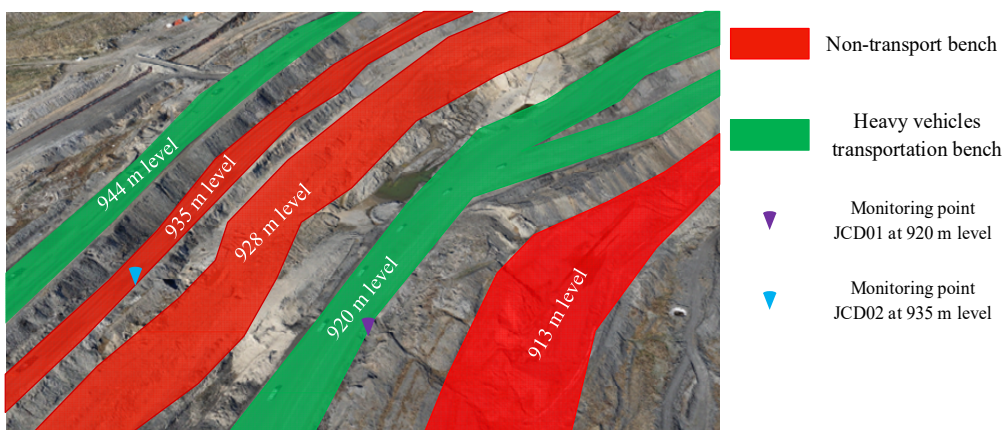


Fig. 19. Different horizontal benches of the north side of Zhahanur open-pit Coal mine; 944 m level, 920 m level have heavy-duty vehicles passing while 935 m level, 928 m and 913 m levels did not experience heavy-duty vehicles passing

heavy loading caused deformation at the 920 m. The monitoring data confirm that vehicle loading had a significant effect on the deformation of the north bench slope of the Zhahanur open-pit coal mine.

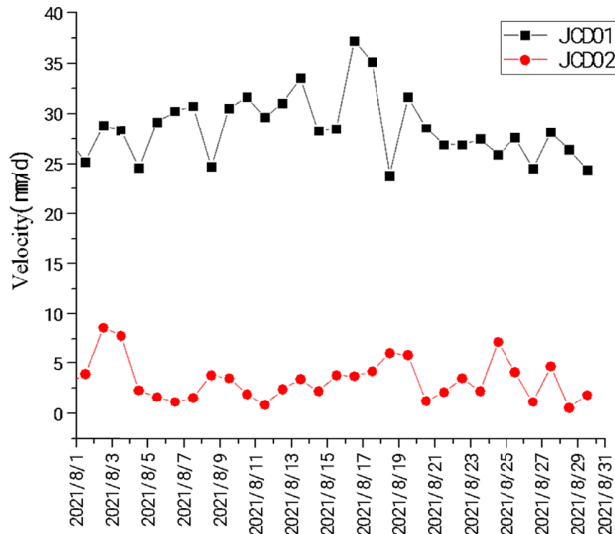


Fig. 20. GNSS monitoring data curves of different levels in the north side of Zhahanur open-pit coal mine. The GNSS monitoring system can monitor the three-dimensional deformation of the bench, and the curve data reflects the three-dimensional deformation of each bench on the north side

6. Conclusions

In the present study, we investigate the impact of cyclic loading from heavy trucks on bench slope stability in the context of open-pit coal mining. To quantify the damage effect on the rock slope induced by cyclic loading, we developed a time-dependent deformation model of rock by incorporating a stress corrosion model into the particle flow code. Based on the established time-dependent model, we studied the effect of the cyclic loading of heavy trucks on bench slope stability. Our results show that the cyclic loading of heavy trucks leads to significant shoulder displacement at the 920 m and 944 m levels, with the shoulder displacement at the 944 m level being the largest at 0.13 m and at the 920 m level being the largest at 0.04 m. Additionally, the cumulative displacement of the non-haulage berm reaches approximately 0.02 m under the combined effects of gravity and cyclic loading. The simulations are consistent with the on-site radar monitoring results, which verifies the reasonability and accuracy of our developed model. By applying the model to simulate the effect of stress corrosion rate acceleration on slope stability, we discovered that the stability of the slope decreased progressively with the increase of the stress corrosion rate. Under the combined effects of gravity and cyclic loading, the 920 m and 944 m levels experienced significant deformations and formed sliding bodies. Our findings suggest that continuous in-situ monitoring of bench slope stability and implementation of control measures are necessary for increased open-pit coal mining safety and efficiency.

Acknowledgement

We would like to acknowledge funding from National Natural Science Foundation of China (42172312, 51974062, 51950410595), and National Key Research and Development Program of China (2017YFC1503100).

References

- [1] R.L. Collins, Frequency Response of Tires Using the Point Contact Theory. *Journal of Aircraft* **9** (6), 427-432 (1972). DOI: <https://doi.org/10.2514/3.59007>
- [2] K.H. Guo, G.F. Ding, Analysis of tire inclusion characteristics and its application in vehicle vibration system modeling. *Automotive Engineering* **02**, 65-71+80 (1999). DOI: <https://doi.org/10.19562/j.chinasae.qcgc.1999.02.001>
- [3] B. Li, Y.F. Gao, D.X. Wei, H.L. Liu, Research on influential depth of vehicle loads and its influencing factors. *Yantu Lixue/Rock and Soil Mechanics* **26**, 310-313 (2005). DOI: <https://doi.org/10.16285/j.rsm.2005.s1.074>
- [4] G. Lan, W. Xu, L. Guo, S. Shi, Research on kinetic effect of vehicular load on subgrade. *Journal of Chengdu University (Natural Science Edition)* **29**, (04) 346-348 (2010).
- [5] T. Kokusho, T. Ishizawa, K. Koizumi, Energy approach to seismically induced slope failure and its application to case histories. *Engineering Geology* **122** (1-2), 115-128 (2011). DOI: <https://doi.org/10.1016/j.enggeo.2011.03.019>
- [6] J. Wartman, R.B. Seed, J.D. Bray, Shaking table modeling of seismically induced deformations in slopes. *Journal of Geotechnical and Geoenvironmental Engineering* **131** (5), 610-622 (2005). DOI: [https://doi.org/10.1061/\(ASCE\)1090-0241\(2005\)131:5\(610\)](https://doi.org/10.1061/(ASCE)1090-0241(2005)131:5(610))
- [7] S.W. Sloan, Lower bound limit analysis using finite elements and linear programming. *International Journal for Numerical and Analytical Methods in Geomechanics* **12** (1), 61-77 (1988). DOI: <https://doi.org/10.1002/nag.1610120105>
- [8] D. Loukidis, P. Bandini, R. Salgado, Stability of seismically loaded slopes using limit analysis. *Géotechnique* **53** (5), 463-479 (2003). DOI: <https://doi.org/10.1680/geot.2003.53.5.463>
- [9] G.H. Kim, K.Z. Cho, I.B. Chyun, G.S. Choi, Dynamic stress analysis of vehicle frame using a nonlinear finite element method. *Ksme International Journal* **17** (10), 1450-1457 (2003). DOI: <https://doi.org/10.1007/bf02982324>
- [10] X. Li, Finite element analysis of slope stability using a nonlinear failure criterion. *Computers and Geotechnics* **34** (3), 127-136 (2007). DOI: <https://doi.org/10.1016/j.compgeo.2006.11.005>
- [11] F. Liu, J. Zhao, Limit analysis of slope stability by rigid finite-element method and linear programming considering rotational failure. *International Journal of Geomechanics* **13** (6), 827-839 (2013). DOI: [https://doi.org/10.1061/\(ASCE\)GM.1943-5622.0000283](https://doi.org/10.1061/(ASCE)GM.1943-5622.0000283)
- [12] G.X. Zhang, Z.X. Yuan, N. Wang, Z.Z. Zhang, P. Gao, Dynamic Response Analysis of Compaction Loess Subgrade. *Construction and Urban Planning*, PTS 1-4, 2013.202-208.
- [13] X.G. Yang, S.C. Chi, Seismic stability of earth-rock dams using finite element limit analysis. *Soil Dynamics and Earthquake Engineering* **64**, 1-10 (2014). DOI: <https://doi.org/10.1016/j.soildyn.2014.04.007>
- [14] M. Blundell, D. Harty, Chapter 4 – Modelling and Analysis of Suspension Systems. In: M. Blundell, D. Harty (Eds.), *The Multibody Systems Approach to Vehicle Dynamics* (Second Edition), Butterworth-Heinemann, Oxford, 2015.185-334.
- [15] Y. Zhang, H. Jiang, G. Bai, B. Han, Coupling action of rainfall and vehicle loads impact on the stability of loess slopes based on the iso-water content layer. *Earthquake Research Advances* **2** (3), (2022). DOI: <https://doi.org/10.1016/j.eqrea.2022.100143>
- [16] L.A. Mejia Camones, E.d.A. Vargas, Jr., R.P. de Figueiredo, R.Q. Velloso, Application of the discrete element method for modeling of rock crack propagation and coalescence in the step-path failure mechanism. *Engineering Geology* **153**, 80-94 (2013). DOI: <https://doi.org/10.1016/j.enggeo.2012.11.013>

- [17] S.S. Behbahani, P. Moarefvand, K. Ahangari, K. Goshtasbi, Unloading scheme of Angooran mine slope by discrete element modeling. *International Journal of Rock Mechanics and Mining Sciences* **64**, 220-227 (2013). DOI: <https://doi.org/10.1016/j.ijrmmms.2013.08.018>
- [18] D. Song, H. Du, Numerical Investigation of the Evolution Process of an Open-Pit Mine Landslide Using Discrete-Element Method. *International Journal of Geomechanics* **23** (6) (2023). DOI: <https://doi.org/10.1061/ijgnai.gmeng-7568>
- [19] Z.Y. Yan, H.E. Ge, J.H. Zhang, X.Q. Wang, G.F. Zhao, Research on vehicle-asphalt pavement interaction and micro-structure by discrete element method. *Mechanics of Advanced Materials and Structures* **29** (27), 6803-6813 (2022). DOI: <https://doi.org/10.1080/15376494.2021.1985664>
- [20] D. Zhang, C.Y. Wu, L.L. Cai, J. Bian, C.E. Yin, Discrete Element Modeling of the Meso-Mechanical Response of Asphalt Pavement under Vehicle Load. *Materials* **15** (21) (2022). DOI: <https://doi.org/10.3390/ma15217808>
- [21] E.T. Brown, J.A. Hudson, Fatigue failure characteristics of some models of jointed rock. *Earthquake Engineering & Structural Dynamics* **2** (4), 379-386 (1973). DOI: <https://doi.org/10.1002/eqe.4290020407>
- [22] S. Yang, Y. Tao, J. Tang, Experimental study of triaxial strength and deformation of single jointed sandstone under cyclic loading. *Journal of China University of Mining & Technology* **49** (05), 819-825 (2020). DOI: <https://doi.org/10.13247/j.cnki.jcumb.001163>
- [23] Y.Y. Cai, X. Tang, L.H. Lin, H.L. Chen, F.D. Gao, G. Li, J. Yu, Strain rate response of damage accumulation of marble under fatigue loading. *Chinese Journal of Geotechnical Engineering* **42** (05), 827-836 (2020). DOI: <https://doi.org/10.11779/CJGE202005004>
- [24] M. Ghamgosar, N. Erarslan, D.J. Williams, Experimental Investigation of Fracture Process Zone in Rocks Damaged Under Cyclic Loadings. *Experimental Mechanics* **57** (1741-2765), 97-113 (2017). DOI: <https://doi.org/10.1007/s11340-016-0216-4>
- [25] M. Ghamgosar, N. Erarslan, D.J. Williams, Experimental Investigation of Fracture Process Zone in Rocks Damaged Under Cyclic Loadings. *Experimental Mechanics* **5** (1), 97-113 (2017). DOI: <https://doi.org/10.1007/s11340-016-0216-4>
- [26] B.K. Atkinson, Subcritical crack growth in geological materials. *Journal of Geophysical Research: Solid Earth* **89** (B6), 4077-4114 (2012). DOI: <https://doi.org/10.1029/JB089iB06p04077>
- [27] N. Brantut, P. Baud, M.J. Heap, P.G. Meredith, Micromechanics of brittle creep in rocks. *Journal of Geophysical Research. Solid Earth* **11** 7(8) (2012). DOI: <https://doi.org/10.1029/2012jb009299>
- [28] P.A. Cundall, O.D.L. Strack, A discrete numerical model for granular assemblies. *Géotechnique* **16** (4), 47-65 (1979). DOI: [https://doi.org/10.1016/0148-9062\(79\)91211-7](https://doi.org/10.1016/0148-9062(79)91211-7)
- [29] B. Zhao, T. Xu, S.Q. Yang, T.F. Fu, Experimental and numerical study of fatigue damage of highly stressed rocks under cyclic loading. *Journal of Central South University (Science and Technology)* **52** (08), 2725-2735 (2021). DOI: <https://doi.org/10.11817/j.issn.1672-7207.2021.08.019>
- [30] G.H. Hu, T. Xu, C.F. Chen, X.K. Yang, A microscopic study of creep and fracturing of brittle rocks based on discrete element method. *Engineering Mechanics* **35** (09), 26-36 (2018). DOI: <https://doi.org/10.6052/j.issn.1000-4750.2017.05.0356>
- [31] D.O. Potyondy, Simulating stress corrosion with a bonded-particle model for rock. *International Journal of Rock Mechanics and Mining Sciences* **44** (5), 677-691 (2007). DOI: <https://doi.org/10.1016/j.ijrmmms.2006.10.002>
- [32] Z.H. Dang, Z.M. Yin, D.S. Wang, M.Y. Fu, Q. Yin, Experimental Study on the Calibration of Microparameters of Dolomite in the Barun Open-Pit Mine on the Basis of the Parallel Bond Model. *Advances In Civil Engineering* **2021** (2021). DOI: <https://doi.org/10.1155/2021/1267536>
- [33] Z.J. Ma, G. Mei, E. Prezioso, Z. Zhang, N.X. Xu, A deep learning approach using graph convolutional networks for slope deformation prediction based on time-series displacement data. *Neural Computing and Applications* **33** (21), 14441-14457 (2021). DOI: <https://doi.org/10.1007/s00521-021-06084-6>
- [34] M. Cross, Sensitivity analysis of shallow planar landslides in residual soils on south Pennine hillslopes. Derbyshire, UK, *Bulletin of Engineering Geology and the Environment* **78** (3), 1855-1872 (2019). DOI: <https://doi.org/10.1007/s10064-017-1195-0>
- [35] Olabode, O. Peter, San, H. Lim, Hydrogeological Assessment of Hydraulic Conductivity on Gully Formation in Erosion Degraded Residual Soil of an Unstable Slope. *Indian Geotechnical Journal* (prepublish) (2022).

- [36] F.Y. Zhang, G. Liu, W.W. Chen, S.Y. Liang, R.S. Chen, W.F. Han, Human-induced landslide on a high cut slope: a case of repeated failures due to multi-excavation. *Journal of Rock Mechanics and Geotechnical Engineering* **4** (04), 367-374 (2012). DOI: <https://doi.org/10.3724/SP.J.1235.2012.00367>
- [37] E.A.G. Marques, D.J. Williams, I.R. Assis, M.F. Leão, Effects of weathering on characteristics of rocks in a sub-tropical climate: weathering morphology, in situ, laboratory and mineralogical characterization. *Environmental Earth Sciences* **76** (17), 602 (2017). DOI: <https://doi.org/10.1007/s12665-017-6936-7>
- [38] T. Bracko, B. Zlender, P. Jelusic, Implementation of Climate Change Effects on Slope Stability Analysis. *Applied Sciences-Basel* **12** (16), (2022). DOI: <https://doi.org/10.3390/app12168171>
- [39] Z.X. Yan, C.M. Yan, H.Y. Wang, Mechanical interaction between roots and soil mass in slope vegetation. *Science China Technological Sciences* **53** (11), 3039-3044 (2010). DOI: <https://doi.org/10.1007/s11431-010-4137-7>
- [40] W.B. Zan, W.J. Zhang, N. Wang, C.C. Zhao, Q. Yang, H. Li, Stability analysis of complex terrain slope based on multi-source point cloud fusion. *Journal of Mountain Science* **19** (9), 2703-2714 (2022). DOI: <https://doi.org/10.1007/s11629-022-7307-8>